Supplemental Information

Unveil the role of structural vacancy in Mn-based Prussian blue analogues for energy storage application

Chongwei Gao,[a] Ming Chen,[b] Jiantao Li,*[c] Xunan Wang,[a] Guobin Zhang,[a] Xi Tan,[b] Shuhua Zhang,[a] Guang Feng,*[b] Dengyun Zhai*[a] and Feiyu Kang*[a]

[a]*Shenzhen Geim Graphene Center, Institute of Materials Research, Tsinghua Shenzhen International Graduate School, Tsinghua University, Shenzhen 518055, China.*
[b]*State Key Laboratory of Coal Combustion and School of Energy and Power Engineering, Huazhong University of Science and Technology, Wuhan 430070, China.*
[c]*Chemical Sciences and Engineering Division, Argonne National Laboratory, Lemont, IL 60439, USA.*

KEYWORDS: Prussian blue; Structural vacancy; Structural design; Alkali metal-ion battery.

Methods

Materials Synthesis

All materials are obtained by a simple co-precipitation in aqueous solutions. The precursor salts used in this work are commercially available without any purification. Typically, MnHCF-IV was synthesized as follows: 3 mmol $MnCl_2$ and 2 mmol $K_4Fe(CN)_6$ were dissolved in 100 mL deionized (DI) water to obtain solution A and solution B respectively. Solution A was followed to be added into solution B slowly with magnetic stirring for 6 h. The mixed solution was aged for another 6 h. The precipitates were centrifugated and washed three times with DI water. Finally, the products were dried under a vacuum at 100 ℃ for 12 h. To obtain H-MnHCF, ethylenediaminetetraacetic acid dipotassium salt dehydrate (EDTA-2K, 10 mmol) was added to solution A, while keeping the other conditions the same. MnHCF-SV was synthesized by replacing $K_4Fe(CN)_6$ in solution B with $K_3Fe(CN)_6$ without adding any chelating agent. For the synthesis of MnHCF-C, potassium citrate (10 mmol) was added to solution A, while maintaining the other conditions as MnHCF-IV. For MnHCF-pSV, $K_4Fe(CN)_6$ was replaced by $K_3Fe(CN)_6$, and the other conditions are the same as MnHCF-C. For the co-reactant method, solution B was composed of $K_3Fe(CN)_6$ and $K_4Fe(CN)_6$ with different molar ratios (1mmol: 2mmol and 2mmol: 1mmol), corresponding to MnHCF-pSV-cL and MnHCF-pSV-cH, respectively. The other conditions maintained the same as MnHCF-C.

Materials Characterizations

The powder X-ray diffraction (XRD) patterns were collected using the reflection mode (Rigaku D/max 2500/PC, Cu-Ka, λ = 1.54056 Å). The XRD patterns were analyzed using the GSAS-II packages.[1] The TEM images were recorded using High-resolution Transmission Electron Microscopy (HRTEM, FEI Tecnai G2 F30). The iDPC-STEM images were obtained using a cold-field-emission spherical aberration corrected transmission electron microscope (Thermo Fisher Scientific, Spectra 300), which was operated at 80 kV. The morphologies of different samples are obtained by scanning electron microscope (SU8010, 5kV). The chemical composition of samples was tested by TGA (Shimadzu DTG-60, Japan) and Inductive Coupled Plasma Emission Spectroscopy (ICP, Arcos II MV). FT-IR was performed using a Nicolet iS50. XPS spectra were collected using PHI Versaprobe 4, with a sputtering time of 90 s using an argon ion beam. The synchrotron-based XAS were measured at beamline 1W1B of Beijing Synchrotron Radiation Facility (BSRF), which was recorded on transmission model. The dates were analyzed using the Athena[2] and HAMA packages.[3]

Electrochemical Characterizations

The cathode slurry was obtained by stirring the active materials, Ketjen black, Carboxymethylcellulose sodium (CMC-Na), and an appropriate amount of deionized water in a weight ratio of 7:2:1. The slurry was coated on Al foil and dried at 100 °C in a vacuum oven overnight. The loading mass was around 1-2 mg cm^{-2}. 1 M lithium hexafluorophosphate ($LiPF_6$) and 1 M sodium hexafluorophosphate ($NaPF_6$) in ethylene carbonate/diethyl carbonate (EC/DEC) (1:1 by volume) were used as electrolytes for the electrochemical test of Li-ion and Na-ion storage, respectively. As for K-ion storage, 2.5 M potassium bis(fluorosulfonyl)imide (KFSI) in triethyl phosphate (TEP) was used as the electrolyte. All the R2032-type coin cells were assembled in a Braun glove box under an Ar atmosphere with contents of oxygen and moisture below 0.1 ppm, using Li/Na/K metal as the counter electrode and glass fiber (Whatman, GF/A) and Celgard membrane (2320) as the separator. The galvanostatic charge/discharge was tested within the voltage range from 2.0 to 4.3V (vs. Li/Li^+ and K/K^+) and 2.0 to 4.2V (vs. Na/Na^+) using land 2001A battery testing system. The galvanostatic intermittent titration technique (GITT) was used to determine the diffusion coefficients of K^+ in different materials. The batteries were charged for 10 min followed by rest steps for 0.5 h with a constant current pulse (10 mA g^{-1}). The K^+ ion diffusion coefficient was calculated using the following equation.

$$D = \frac{4}{\Pi t}\left(\frac{r_s}{3}\right)^2\left(\frac{\Delta V_s}{\Delta V_t}\right)^2 \quad (1)$$

τ is the time duration of the pulse, r_s is the radius of the particle, the voltage changes of ΔV_s and ΔV_t can be obtained from the GITT curves.[4] We assumed the solid phase consists of spherical particles with radius r_s, which was calculated by the TEM images. There will be some errors coming from the segregation of the particles and the particles are not completely uniform. However, the actual electrolyte contact area is hard to estimate because of the nanopore structure of PBAs. Considering the structural similarity, the errors caused by r_s can be accepted and the calculated K^+ diffusion coefficient can be used for comparative analysis. SOC-independent in-situ EIS was performed in Solartron 1470E workstation. A current density of 20 mA g^{-1} was applied for the charging and discharging processes. Potentiostatic EIS measurements in the 0.01 Hz to 100 kHz range were carried out with an amplitude of 10 mV. The DRT deconvolution was conducted by DRTtools online algorithm, developed by Professor Francesco Ciucci's team.[5]

Calculation Methods

DFT calculation

The computational calculations were handled using the density functional theory (DFT) in Vienna ab-initio simulation package (VASP)[6] with Perdew-Burke-Ernzerhof (PBE) exchange-correlation functions of generalized gradient approximation (GGA).[7] The projector augmented wave (PAW) method[8] with a cutoff energy of 520 eV was used to describe the interaction between nuclei and electrons. The dipole correction and spin polarization were added for the calculations. The effective single parameters of U–J for Mn and Fe are 5.0 eV and 4.3 eV, respectively, according to the preview literature.[9] The convergence criteria for energy and force were set as 10^{-5} eV and 0.02 eV/Å, respectively. The oxidation stabilities, characterized by the highest occupied molecular orbital (HOMO), of water and water coordinated with Mn^{2+}, were performed with Gaussian 09 program (revision, D.01) via B3LYP/6-311G.[10]

Supplementary Notes

Supplementary Note 1 | Analysis of XANES spectra.

For the octahedral field with six coordination, dipole radiative transitions of 1s→3d are not allowed by the selection rules. However, dipole radiative transitions of 1s→3d are allowed in the tetrahedral field with four coordination.[11] As marked by the rectangle in **Fig. 2(b)**, there is no sign in these areas for H-MnHCF and MnHCF-IV, indicating an O_h geometry in the Mn site. Two weak peaks at about 6526 and 6529 eV can be observed in MnHCF-SV, more likely corresponding to 1s→3d of Mn with T_d geometry. The low peak intensity is likely due to the effect of coordinated water around Mn atoms, and the half-filled 3d orbitals will also lead to weak absorption. A strong shoulder peak at around 6540.5 eV is obvious in MnHCF-SV, corresponding to the radiative transitions of 1s→4p_z, suggesting a lack of coordination along the z-axis in O_h and leading to D_{4h} geometry. However, the shoulder peak is weak in H-MnHCF and MnHCF-IV, indicating an O_h geometry of Mn atoms in both structures. In addition, the shape response area of MnHCF-SV is different from H-MnHCF and MnHCF-IV, further verifying that the coordination environment is changed.

In short, for MnHCF-SV, T_d and D_{4h} likely coexist in the Mn site, corresponding to symmetric and asymmetric vacancies, as shown in the inset of **Fig. 1(b)**. Combining the vacancy fraction of 1/3 with the geometry analysis, a reasonable distribution of SV in MnHCF-SV is shown in **Fig. S6**. Neighboring vacancies form long channels, in favor of ion diffusion.

Supplementary Note 2 | DRT peak assignment

Despite employing the highly precise analysis method of DRT, obtaining signals from the cathode of PBAs remains challenging when utilizing the traditional coin cell for EIS testing. Thus, all tests were conducted using a three-electrode cell. The comparison is shown in **Fig. S23**. Initially, a K|K symmetric cell was assembled. Through DRT analysis, three distinct peaks were observed, corresponding to contact resistance, SEI impedance (R_{SEI}), and charge transfer resistance (R_{ct}) of K, respectively (**Fig. S23(a)**). In the Steel|K cell (**Fig. S23(b)**), only the SEI impedance from the side of the K anode and the system's contact resistance can be observed. The absence of R_{ct} can be attributed to the extremely low exchange current density resulting from the electrochemical inertness of steel. In the MnHCF-C|K cell (**Fig. S23(c)**), the obtained DRT spectrum was entirely consistent with the K|K symmetric cell. Even with efforts to minimize the mass of K metal, no signals were observed from the PBA electrode. This is attributed to the fact that EIS is more responsive to the most sluggish reactions in the system. When testing with a three-electrode cell, impedance signals from the working electrode side can be accurately obtained, as shown in **Fig. S23(d)-(f)**. For K metal as the working electrode, the obtained DRT peaks are consistent with those in the symmetric cell, corresponding to contact resistance, R_{SEI}, and R_{ct}. Using stainless steel as the working electrode effectively eliminates R_{SEI} from the potassium electrode side, leaving only the contact resistance. When MnHCF-C is the working electrode, a new peak appears at a higher time constant position, corresponding to the initial R_{ct} of MnHCF-C. The peak in the range from 10^{-2} to 10^{-1} is likely associated with R_{CEI}. As this peak remains relatively constant during cycling, we do not analyze it extensively. Instead, we focus on the charge transfer portion to investigate the reaction processes at the interface.

Supplementary Note 3 | Analysis of the change of DRT peaks

For MnHCF-C, the evolution of R_{ct} can be divided into four reversible stages (**Fig. 6(d)**). In Stage 1, R_{ct} remains unchanged in position, while the impedance gradually decreases. During this stage, the time constant stays constant, indicating a consistent interface structure. As the voltage rises, the reaction driving force strengthens, leading to a reduction in impedance. Hence, this stage corresponds to the transition of Fe^{2+} to Fe^{3+} within the single monoclinic phase. In Stage 2, the R_{ct} peak undergoes a rightward shift. This can be attributed to the structural transition from the initial monoclinic to the cubic phase due to the difference in double-layer capacitance (Cdl) at the interfaces between the monoclinic and cubic phases. Hence, this stage corresponds to the transition of Fe^{2+} to Fe^{3+} during the coexistence stage of the monoclinic and cubic phases. In Stage 3, the cubic phase dominates the interface structure, leading to the unchanged peak position of R_{ct}. Combining the charge-discharge curves, MnHCF-C undergoes the first charging plateau, indicating the transition from Fe^{2+} to Fe^{3+} within the cubic phase. In Stage 4, the peak position of R_{ct} shifts rightward once again, indicating another interface structural change. This can be attributed to the transition from cubic to tetragonal, induced by the oxidation from Mn^{2+} to Mn^{3+}. However, the interfacial tetragonal phase is unstable followed by a leftward shift of R_{ct} peak position, accompanied by a rapid increase in impedance. This observation may be associated with the high-voltage decomposition reactions at the interface, as it is non-reversible during the subsequent discharge process. The discharge process is essentially the inverse from Stage 4 to Stage 1.

For MnHCF-SV (**Fig. S24(b)**), the time constant of R_{ct} remains largely unchanged throughout the charge and discharge process, indicating that the interface structure remains unchanged. Combining the previous electrochemical analyses, this R_{ct} corresponds to the Fe^{2+}/Fe^{3+} transition within the single cubic phase interface.

For MnHCF-pSV-cL and MnHCF-pSV-cH (**Fig. S24(a)** and **6(d)**), these samples generally maintain the interface reaction processes observed in MnHCF-C, but with a weakened shift in the time constant, especially during the cubic to tetragonal transition at high voltages. In addition, there is a significant increase in the proportion of Stage 3, attributed to the inhibition of JT-distortion with the help of pSV, allowing more Mn^{2+}/Mn^{3+} transformation within the cubic phase. The irreversible peak shift at high voltage decreases, indicating a reduced side reaction.

For MnHCF-pSV (**Fig. 6(d)**), the interface properties are similar to MnHCF-SV. After the initial right shift of R_{ct} peak, the peak position of R_{ct} maintains the same without shifting at high voltage, indicating the disappearance of the tetragonal phase and side reaction.

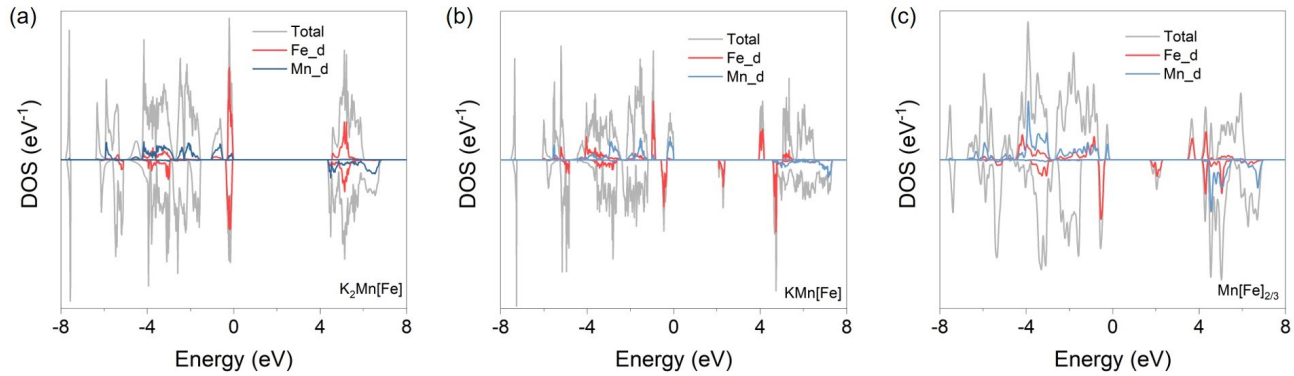

Fig. S1 DOS of (a) $K_2Mn[Fe]$, (b) KMn[Fe], and (c) $Mn[Fe]_{2/3}$. The curves include total DOS (gray) and partial DOS of Mn d orbital (blue) and Fe d orbital (red).

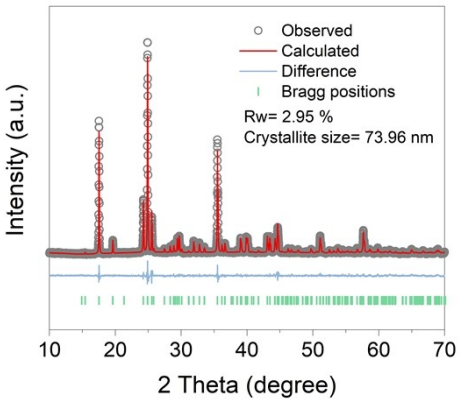

Fig. S2 Rietveld refinement based on the XRD patterns of H-MnHCF.

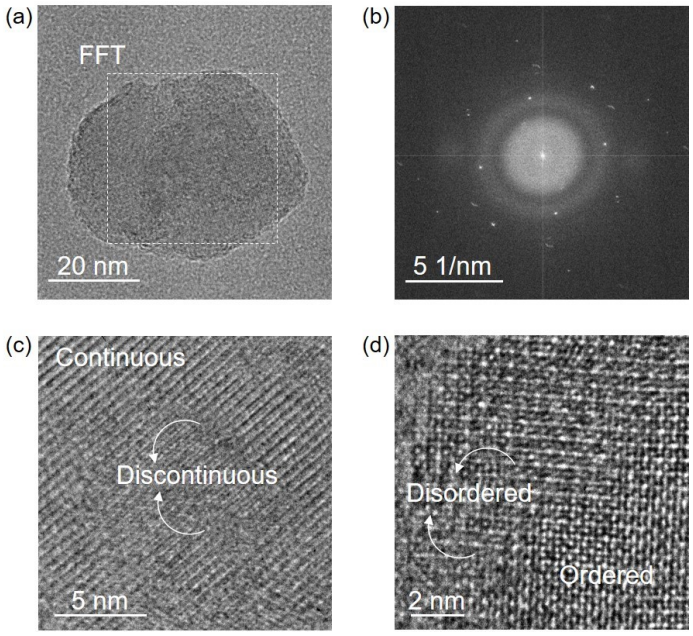

Fig. S3 (a) TEM image, (b) corresponding FFT image, and (c-d) HRTEM images of MnHCF-IV.

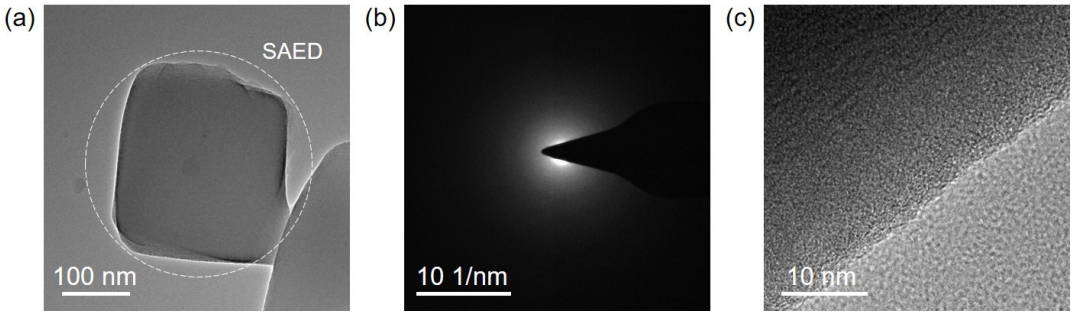

Fig. S4 (a) TEM image, (b) corresponding SAED image, and (c) HRTEM images of MnHCF-SV.

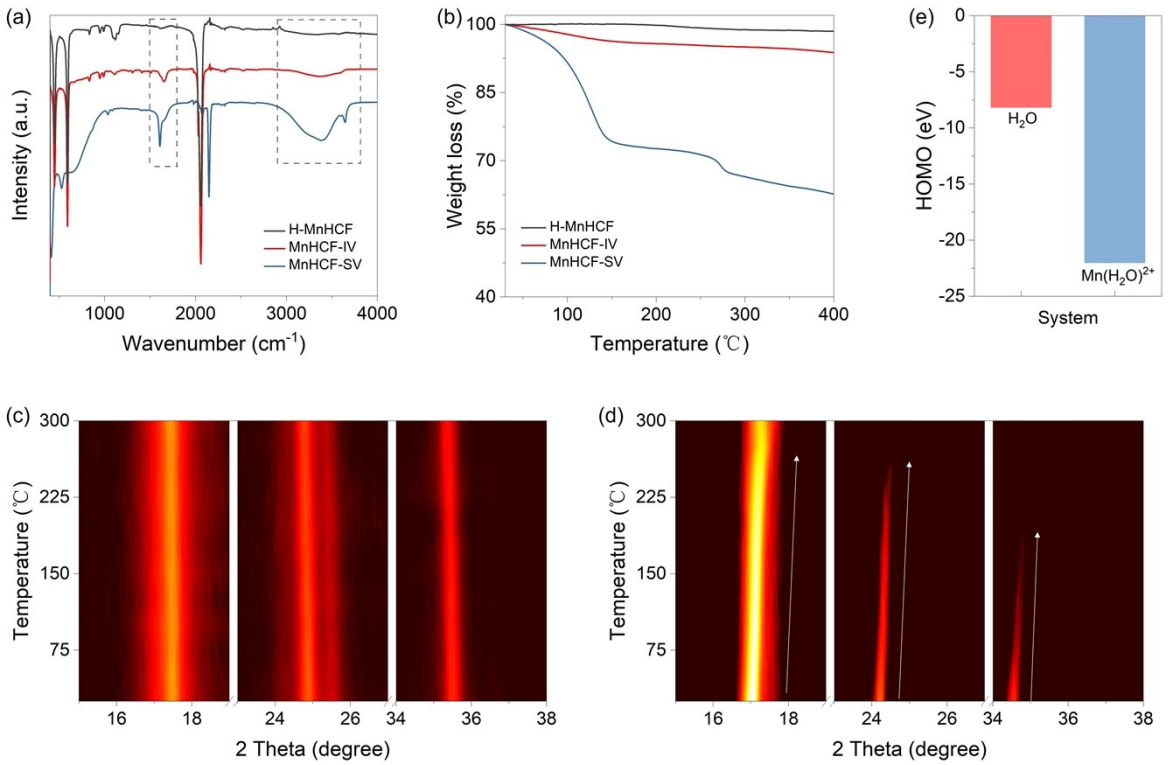

Fig. S5 Characterization of water within the structure. (a) FT-IR spectra and (b) TGA curves of H-MnHCF, MnHCF-IV, and MnHCF-SV. *In-situ* temperature-dependent XRD patterns of (c) MnHCF-IV and (d) MnHCF-SV. (e) Calculated HOMO energy level of H_2O and $Mn(H_2O)^{2+}$ by DFT calculations.

As shown in **Fig. S5**, a single peak around 2067 cm^{-1} can be observed in H-MnHCF and MnHCF-IV, which corresponds to the stretching vibration of C≡N.[12] The peak shifted towards a higher wavenumber in MnHCF-SV due to the strong electron-withdrawing property of Fe^{3+} (connected to C atoms) than Fe^{2+} in H-MnHCF and MnHCF-IV. The peaks from around 2900 to 3800 cm^{-1} in the FT-IR spectra belong to the O-H stretching modes, and the peaks around 1600 cm^{-1} belong to the bending vibrations of water. [13] For H-MnHCF, almost no water can be detected in the FT-IR spectra. Only a broad stretching band in the region of 3150–3350 cm^{-1} is detected in MnHCF-IV, which corresponds to zeolitic water. For MnHCF-SV, a narrow band at 3700 cm^{-1} can be assigned to coordinated water, indicating that water has a strong interaction with the lattice within structural vacancy. The different forms of water in MnHCF-IV and MnHCF-SV can be attributed to the distinct chemical environments of IV and SV, as demonstrated by XAS. Coordinated water helps shield the positive charge of the exposed Mn^{2+} with low coordination numbers in the presence of the SV.

In-situ temperature-dependent XRD and TGA curves were further used to verify the above results (**Fig. S5(b-d)**). For MnHCF-IV, the crystal structure remained stable after removing the water. However, As the temperature gradually increased to about 200°C, the intensity of the diffraction peaks of MnHCF-SV progressively weakened, corresponding to the removal of coordinated water.

DFT calculations were conducted to investigate the risk of coordinated water decomposition in MnHCF-SV (**Fig. S5(e)**). The results show that the highest occupied molecular orbital (HOMO) energy of $Mn(H_2O)^{2+}$ is significantly lower than that of H_2O (from -8.20 eV to -22.04 eV), suggesting that the coordinated water has excellent antioxidative properties. The calculated HOMO energy level is even far below those of commonly used solvents such as ethylene carbonate (EC, -8.45 eV),[14] diethyl carbonate (DEC, -7.67 eV),[14] and triethyl phosphate (TEP, -8.0 eV),[15] indicating the difficulty of coordinated water oxidation within the normal voltage window.

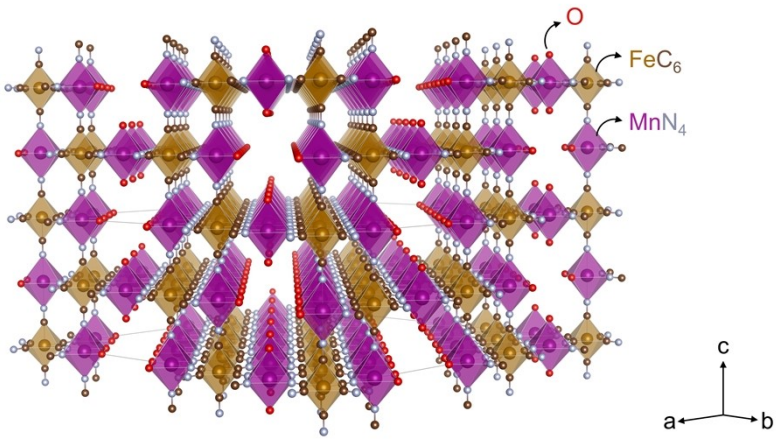

Fig. S6 Schematic structure of MnHCF-SV with long channels formed by neighboring vacancies.

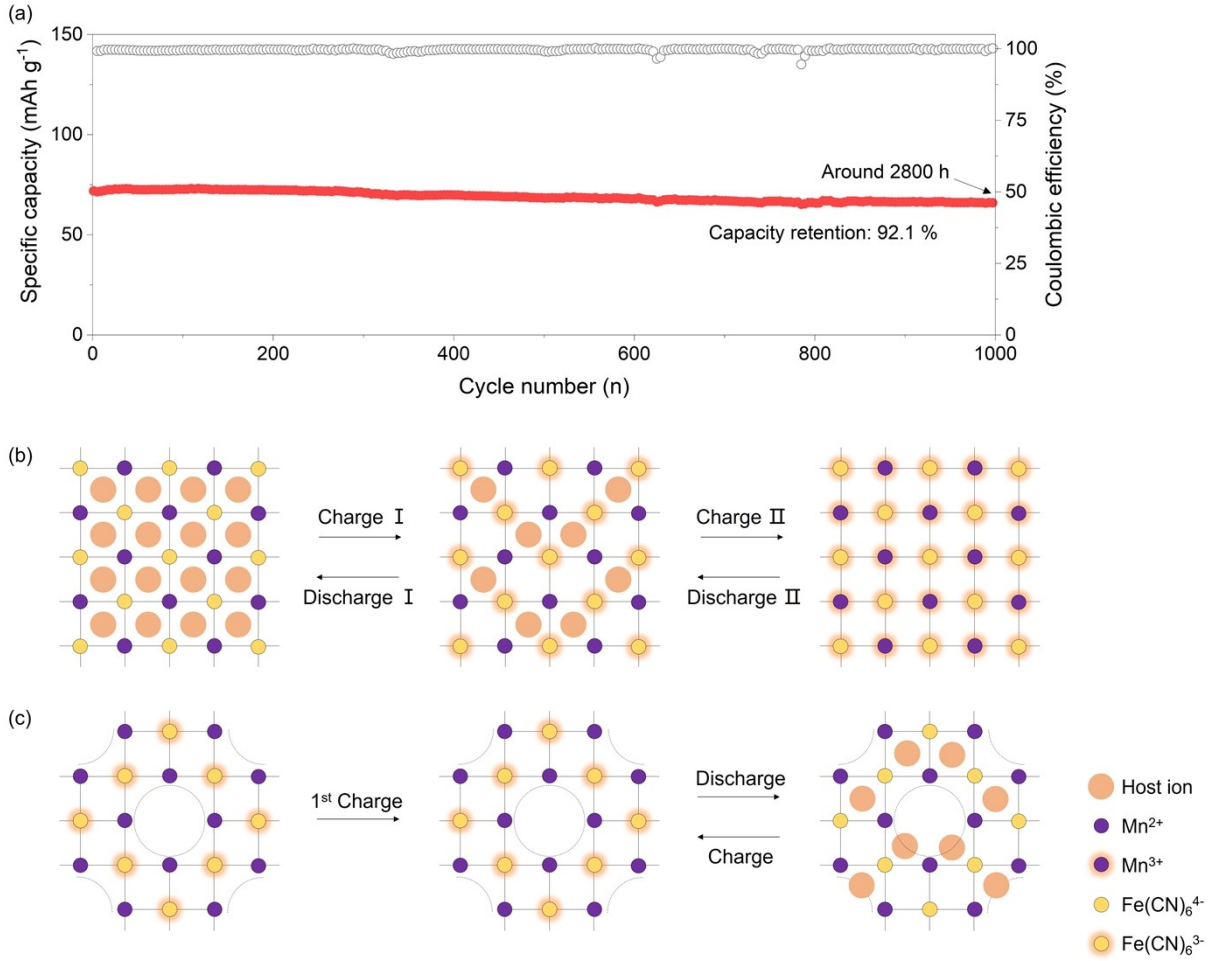

Fig. S7 (a) Long-term cyclic performance of MnHCF-SV at 50 mA g^{-1}. Storage mechanism analysis of (b) normal K^+-containing MnHCF and (c) MnHCF-SV.

As shown in **Fig. S7(b)**, normal $K_2Mn[Fe]$ has an equal quantity between initial K^+ and redox couples (e.g. Fe^{2+}/Fe^{3+} and Mn^{2+}/Mn^{3+}). In contrast, the formation of ordered SVs results in the absence of K^+ in the initial structure of MnHCF-SV, creating an unequal relationship with the redox couples (**Fig. S7(c)**). Therefore, although the valance of Mn is +2 in the initial structure, it remains inactive without an extractable host ion for 1st charge. During the 1st discharge, only high-valance Fe^{3+} can be reduced, and equal ions from the electrolyte are inserted. In the subsequent cycles, Mn^{2+} is always inactive.

The theoretical capacity of MnHCF-SV is calculated to be 76.95 mAh g^{-1} based on the reaction equation (1):

$$Mn_3[Fe(CN)_6]_2 \cdot 6H_2O + 2e^- + 2K^+ \rightleftharpoons K_2Mn_3[Fe(CN)_6]_2 \cdot 6H_2O \quad (1)$$

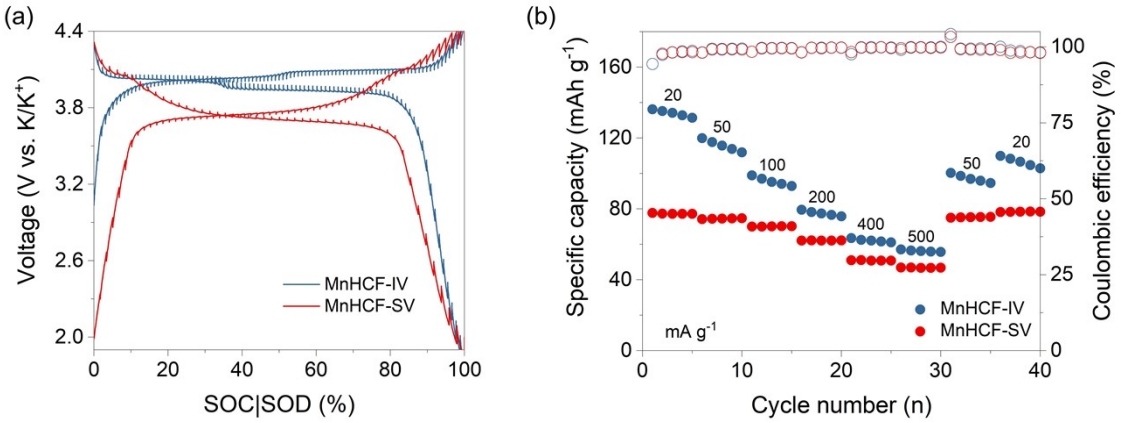

Fig. S8 (a) GITT curves of MnHCF-IV and MnHCF-SV. (b) Rate performance of MnHCF-IV and MnHCF-SV.

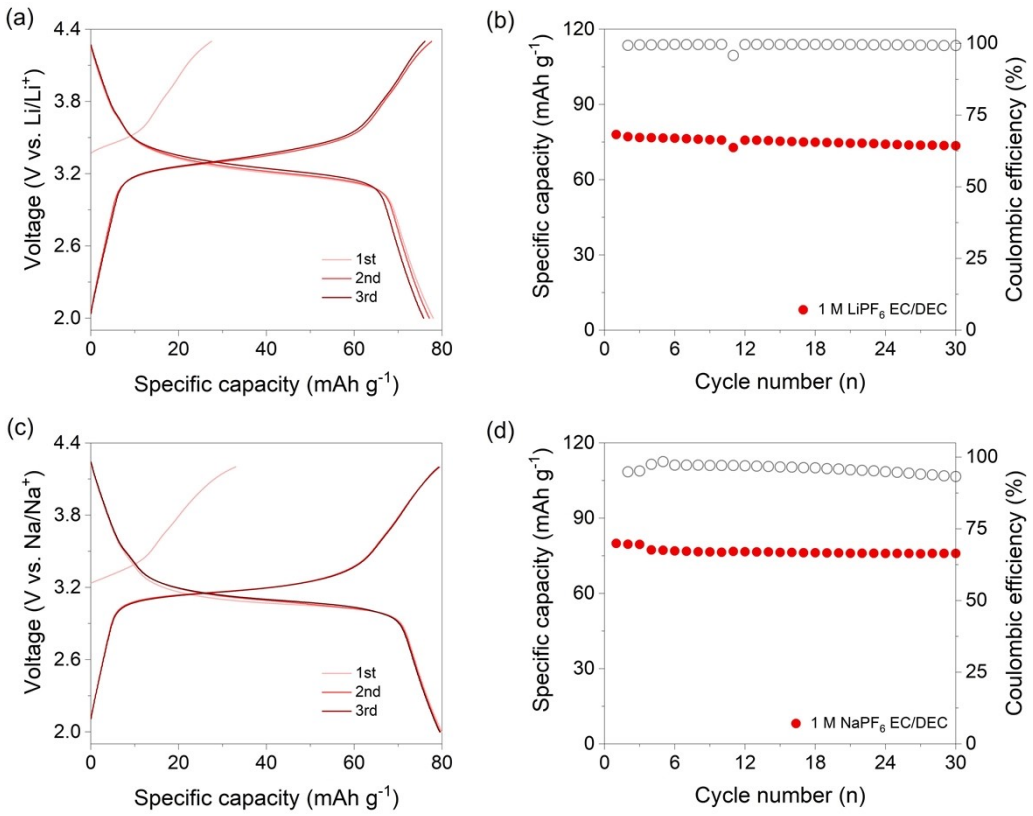

Fig. S9 (a) Charge-discharge curves and (b) Cyclic performance of MnHCF-SV in 1 M $LiPF_6$ EC/DEC. (c) Charge-discharge curves and (d) Cyclic performance of MnHCF-SV in 1 M $NaPF_6$ EC/DEC.

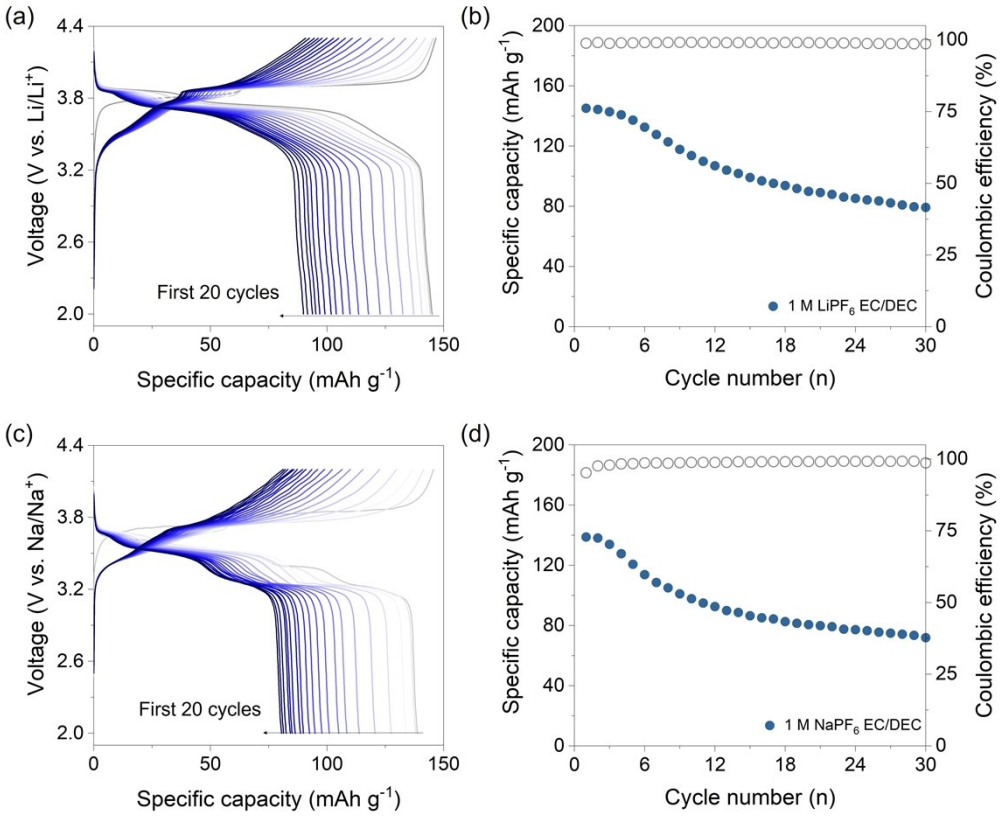

Fig. S10 (a) Charge-discharge curves and (b) Cyclic performance of MnHCF-IV in 1 M $LiPF_6$ EC/DEC. (c) Charge-discharge curves and (d) Cyclic performance of MnHCF-IV in 1 M $NaPF_6$ EC/DEC.

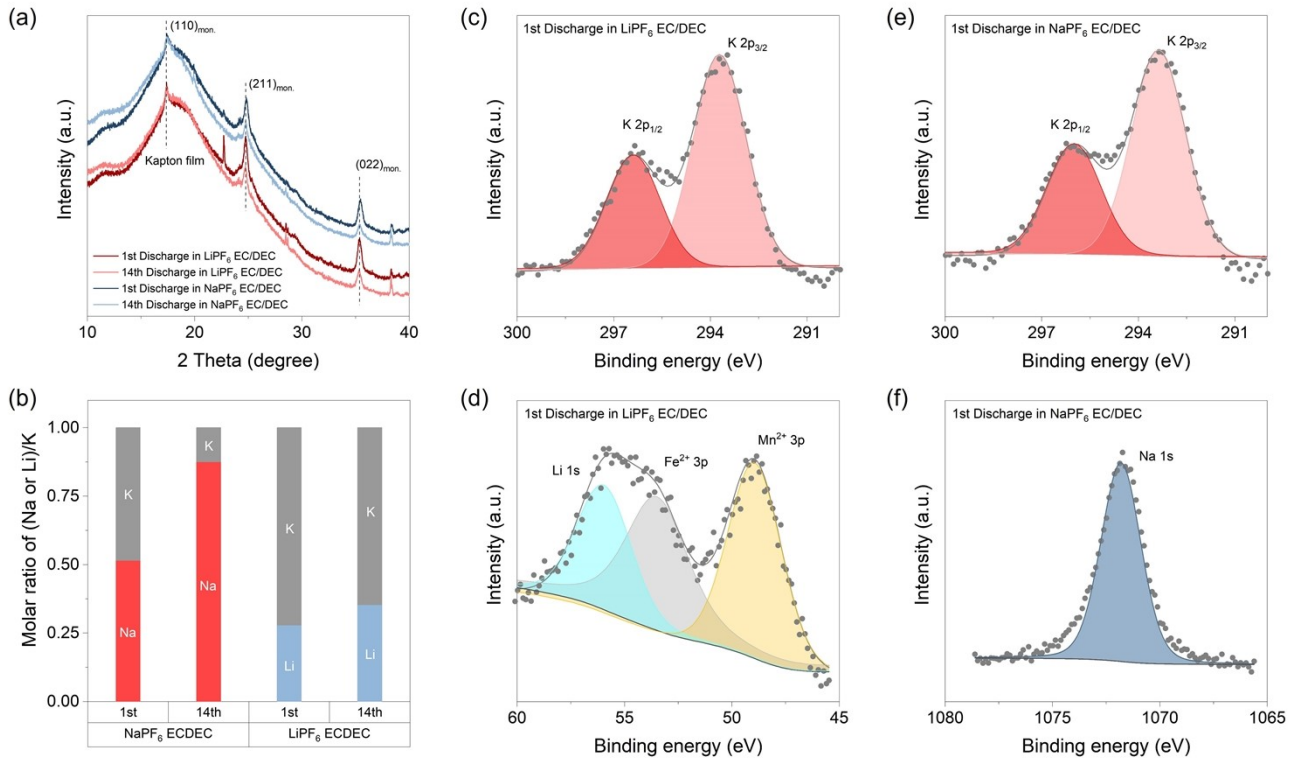

Fig. S11 Investigating the ion insertion behavior of MnHCF-IV in 1 M $LiPF_6$ EC/DEC and 1 M $NaPF_6$ EC/DEC electrolytes. (a) XRD patterns of MnHCF-IV after the 1st and 14th cycles in $LiPF_6$ EC/DEC and $NaPF_6$ EC/DEC electrolytes, respectively. (b) Corresponding (Na or Li)/K molar ratios obtained from ICP analysis. (c) K 2p and (d) Li 1s XPS spectra of MnHCF-IV after the first cycle in $LiPF_6$ EC/DEC. (e) K 2p and (f) Na 1s XPS spectra of MnHCF-IV after the first cycle in $NaPF_6$ EC/DEC.

Due to the presence of K^+ in the initial structure of MnHCF-IV, the ion insertion behavior during cycling in 1 M $LiPF_6$ EC/DEC and 1 M $NaPF_6$ EC/DEC electrolytes was further investigated. As shown in **Fig. S11(a)**, regardless of whether $NaPF_6$ ECDEC or $LiPF_6$ ECDEC electrolyte was used, MnHCF-IV exhibited a monoclinic phase at full-discharge states after cycles. The diminishing intensity of the diffraction peaks indicated structural instability in MnHCF-IV.

The ICP results indicated that during the initial discharge in 1 M $NaPF_6$ EC/DEC, co-insertion of Na^+ and K^+ occurred, with a Na/K molar ratio of approximately 1:1. By the 14th cycle, Na^+ became predominant, as shown in **Fig. S11(b)**.

In 1 M $LiPF_6$ ECDEC electrolyte, the co-insertion molar ratio of Li^+ and K^+ remained around 0.3 (**Fig. S11(b)**). X-ray photoelectron spectroscopy (XPS) analysis further demonstrated the presence of K/Li and K/Na signals, confirming the co-insertion mechanism in both electrolytes (**Fig. S11(c-f)**).

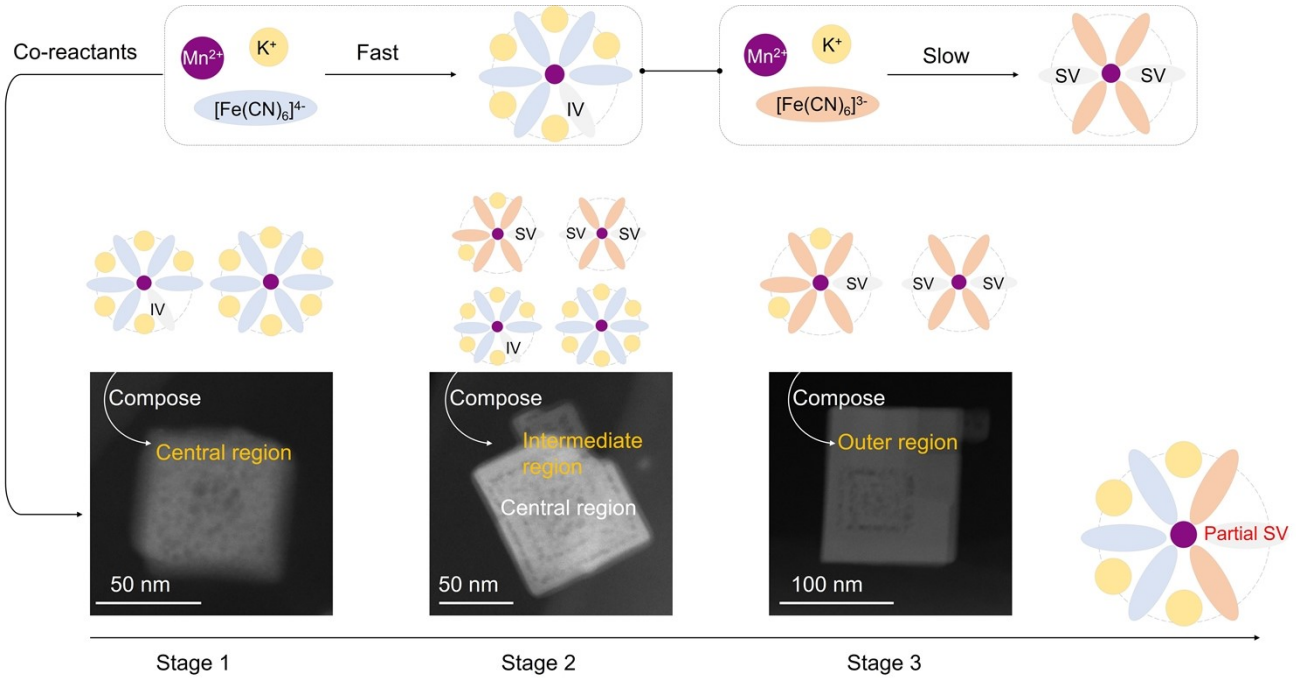

Fig. S12 Reaction process of the co-reactant method confirmed by HADDF-STEM images.

$[Fe(CN)_6]^{4-}$ and $[Fe(CN)_6]^{3-}$ tended to generate K^+-containing MnHCF and SV-containing MnHCF, respectively, as demonstrated in **Section 1**. Due to the faster reaction rate of $[Fe(CN)_6]^{4-}$ than that of $[Fe(CN)_6]^{3-}$, the two reagents participated in different stages of growth, as confirmed by TEM.

In stage 1, $Fe(CN)_6^{4-}$ was the primary reactant to realize the K-rich structure in the central region. Due to the lattice contraction induced by K^+, which can be proved by XRD results, the structure became more localization and eventually formed a 'chaotic' morphology.

In stage 2, $Fe(CN)_6^{3-}$ co-participated in the particle growth along with $Fe(CN)_6^{4-}$ in the intermediate region, introducing structural vacancies. This resulted in the formation of outer shells that are morphologically distinct from the interior, as the SVs effectively alleviate lattice contraction.

In stage 3, $Fe(CN)_6^{3-}$ served as the primary reactant, ultimately leading to the formation of an outer region dominated by SVs

After these three stages, the final products MnHCF-pSV-cH and MnHCF-pSV-cL were obtained, determined by the ratio of the reactants.

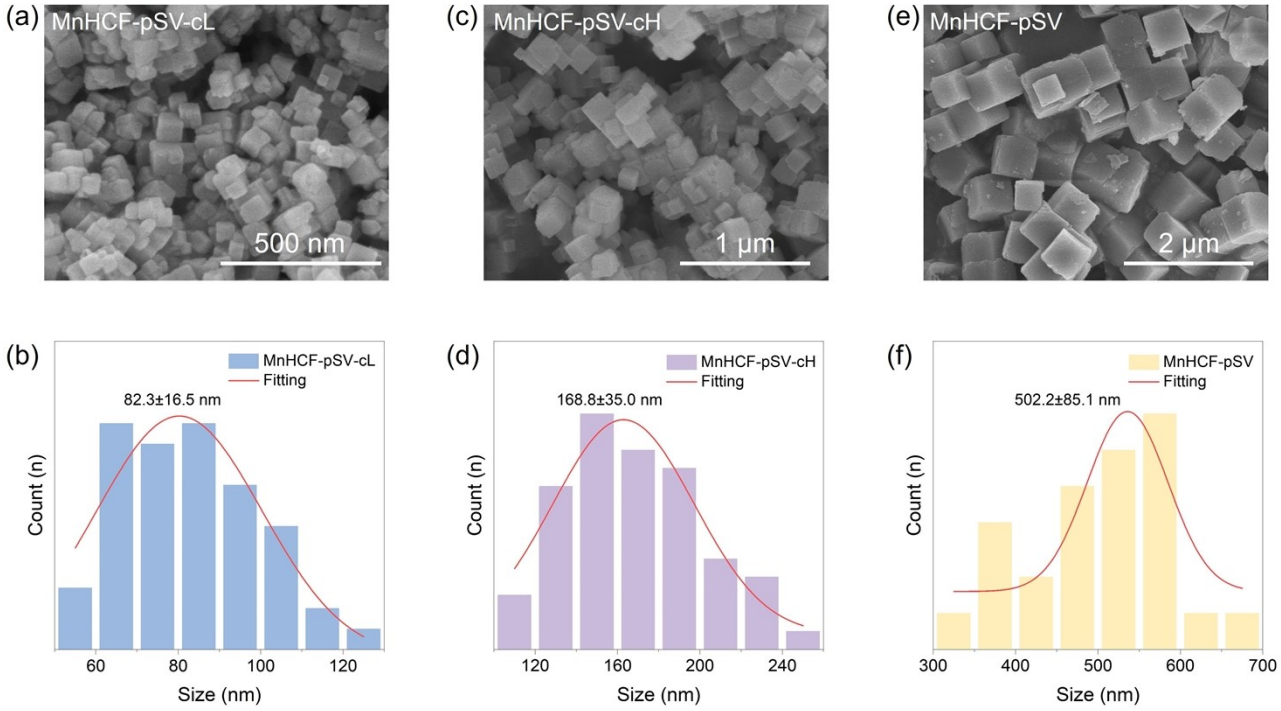

Fig. S13 SEM images and corresponding size distribution of (a, b) MnHCF-pSV-cL, (c, d) MnHCF-pSV-cH, and (e, f) MnHCF-pSV.

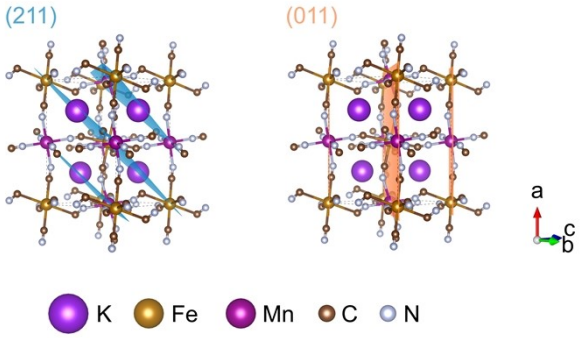

Fig. S14 Schematic diagrams of (211) and (011) crystal plane.

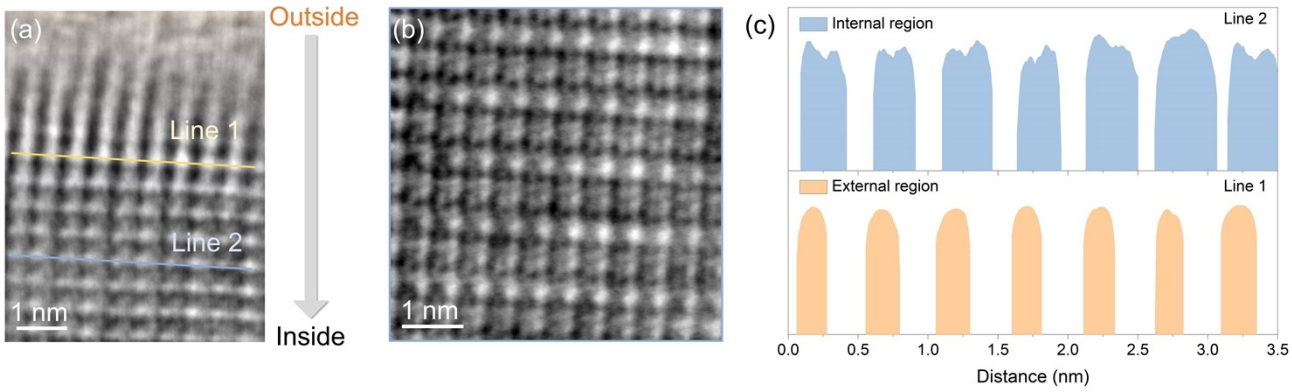

Fig. S15 Microstructure characterization of MnHCF-pSV-cH. (a) iDPC-STEM image and (b) zoom-in image in the internal region. (c) Line profiles along line 1 and line 2, marked in (a).

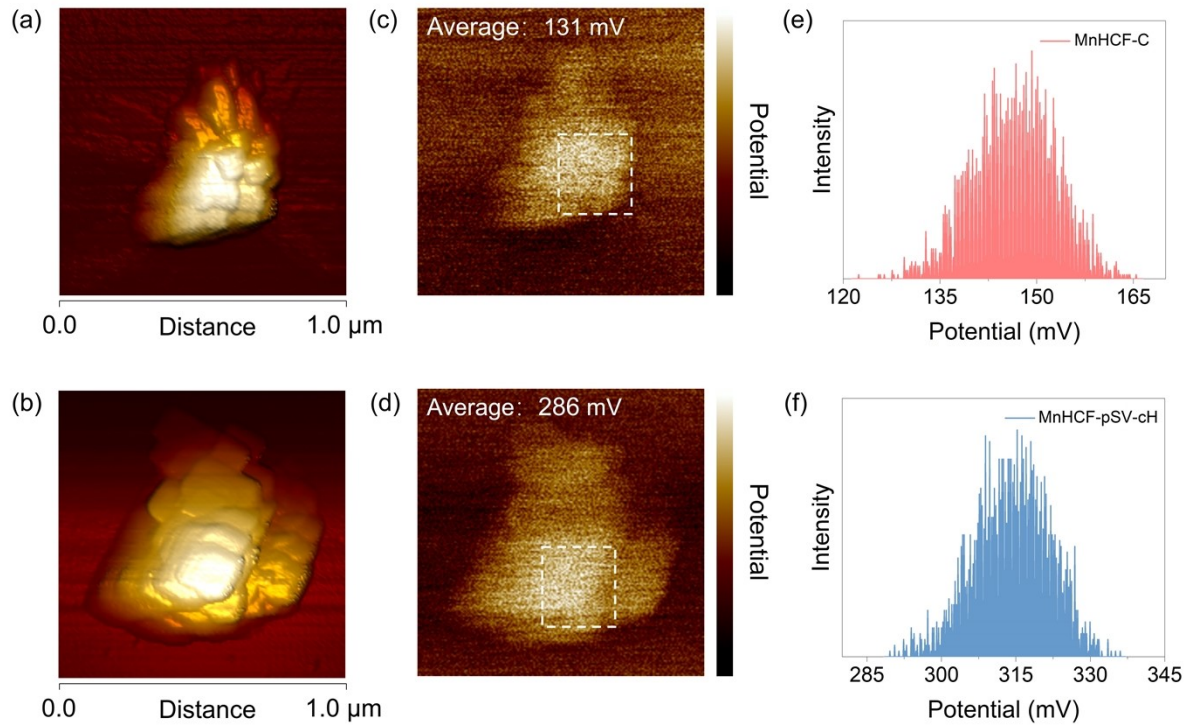

Fig. S16 AFM images of (a) MnHCF-C and (b) MnHCF-pSV-cH. KPFM images of (c) MnHCF-C and (d) MnHCF-pSV-cH. (c) and (f) The corresponding surface potential analysis within the rectangles in (c) and (d).

AFM images (**Fig. S16(a)** and **(b)**) indicate an increase in particle size using the co-reactant method due to the participation of $Fe(CN)_6^{3-}$. **Fig. S16(c)** and **(d)** show the corresponding KPFM images. The average surface potential increased from 131 mV to 286 mV. The surface potential distribution profiles within the marked rectangle are illustrated in **Fig. S16(e)** and **(f)**. The obvious increase in surface potential observed in MnHCF-pSV-cH proves that the surface structure is notably changed with the introduction of SV.

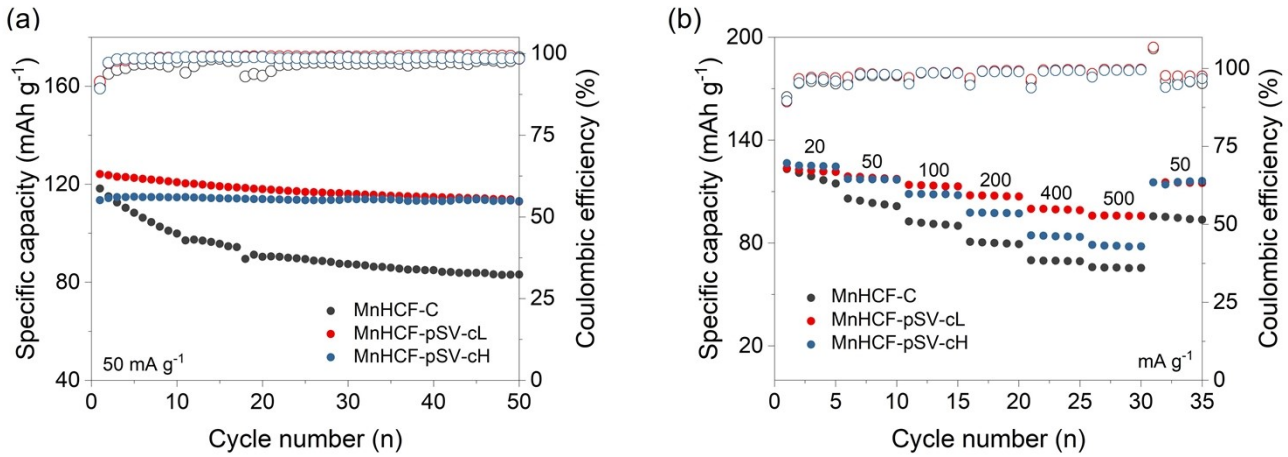

Fig. S17 (a) Cyclic and (b) rate performance of MnHCF-C, MnHCF-pSV-cL, and MnHCF-pSV-cH.

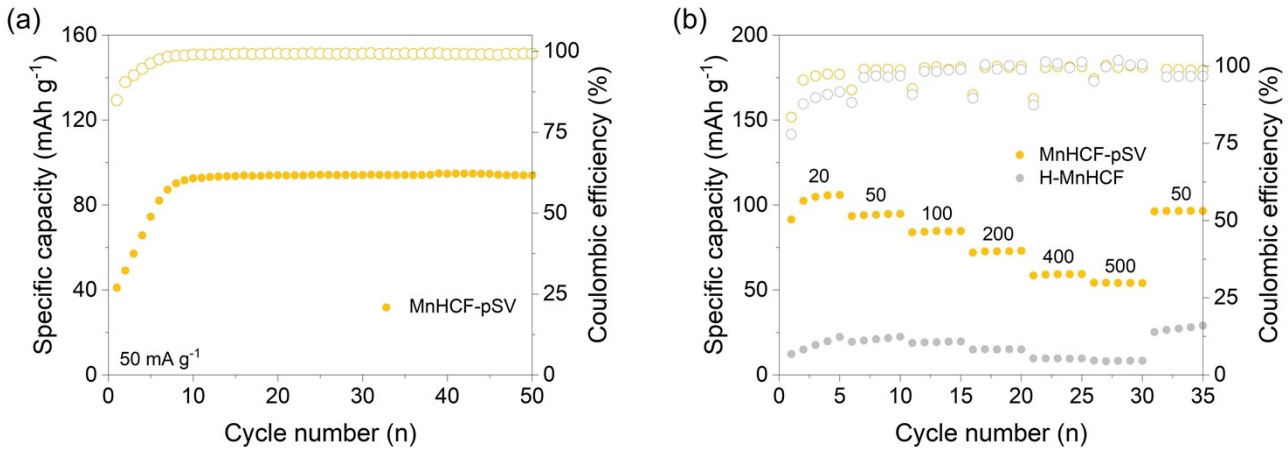

Fig. S18 (a) Cyclic and (b) rate performance of MnHCF-pSV.

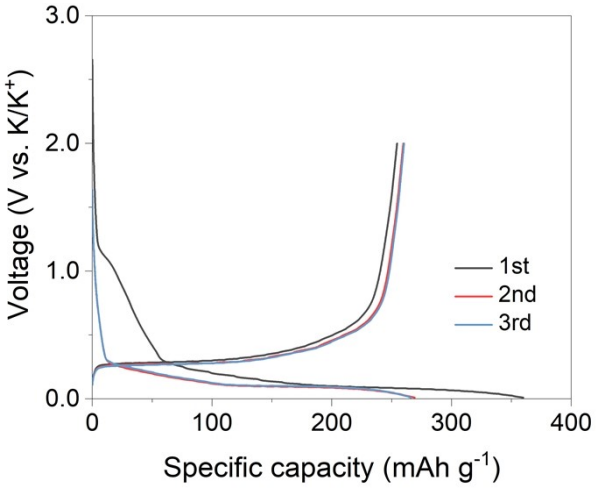

Fig. S19 Charge-discharge curves of NG at 50 mA g^{-1}. NG was pre-cycled three times and then assembled into the full cell.

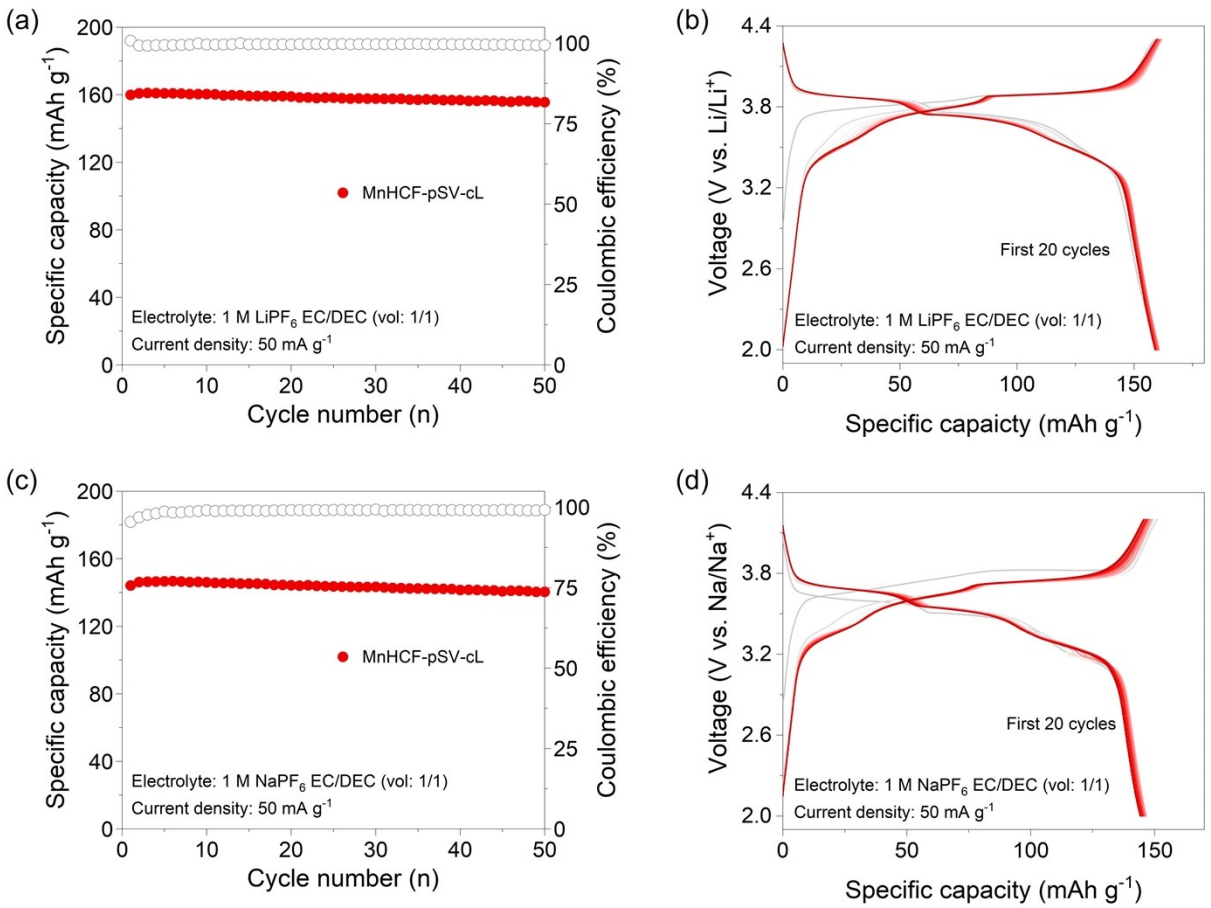

Fig. S20 (a) Cyclic performance and (b) charge-discharge curves of MnHCF-pSV-cL in 1 M $LiPF_6$ EC/DEC. (c) Cyclic performance and (d) charge-discharge curves of MnHCF-pSV-cL in 1 M $NaPF_6$ EC/DEC.

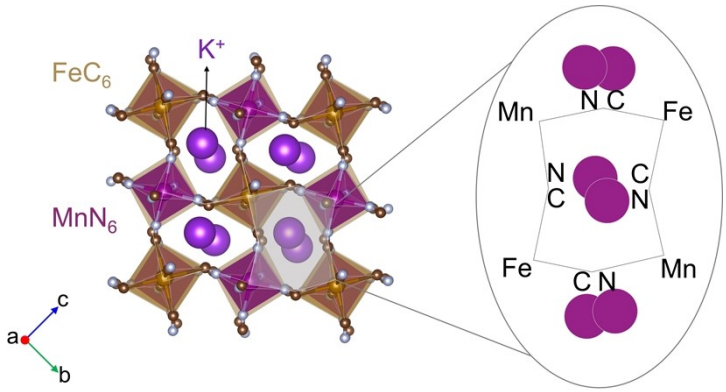

Fig. S21 Initial monoclinic structure of K^+-rich MnHCF.

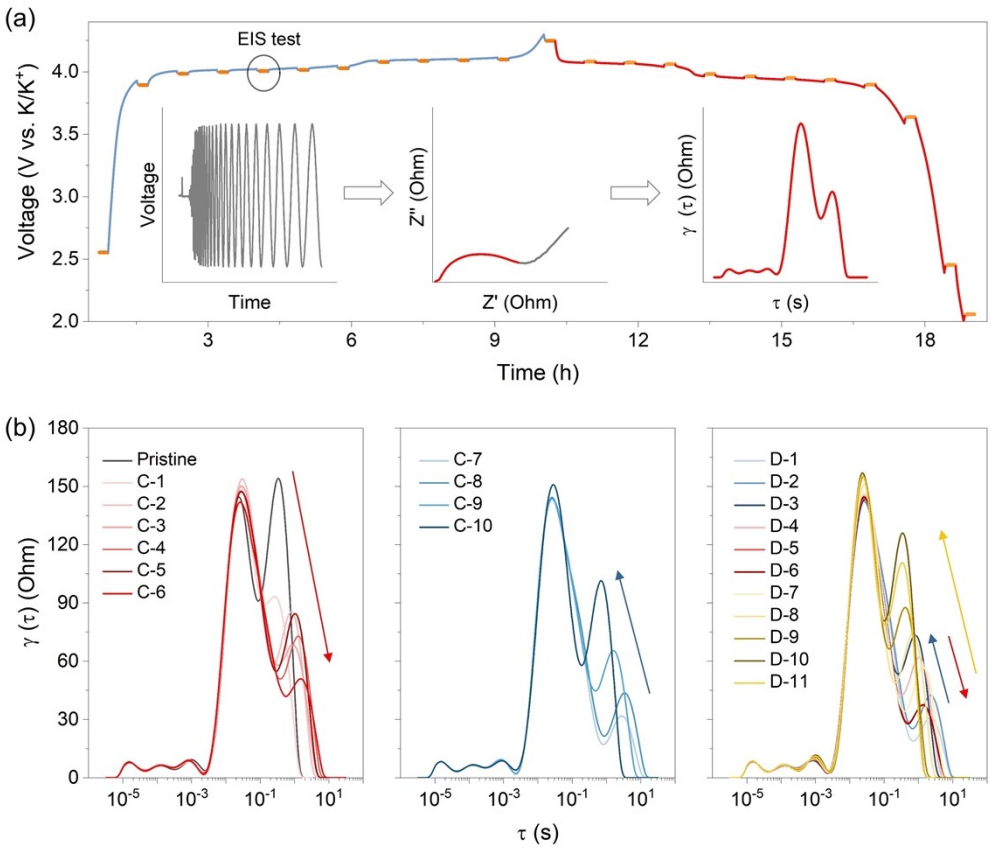

Fig. S22 (a) SOC-independent *in-situ* EIS testing and DRT data processing workflow, including data measurement, EIS preprocessing, and DRT transformation, exemplified by MnHCF-C with identical procedures applied to other samples. (b) DRT plots of MnHCF-C during the first cycle.

As illustrated in **Fig. 22(a)**, EIS tests were performed at regular intervals during the cycling process. A series of EIS spectra were obtained, and after pre-processing to eliminate divergent components, they were ultimately transformed into a DRT plot. The DRT is a model-free method that avoids erroneous pre-modeling of the equivalent circuit model (ECM), thereby increasing resolution in analyzing complex electrochemical processes.[16, 17] All tests were conducted using a three-electrode cell.

Taking MnHCF-C as an example, its R_{ct} exhibits dynamic changes during charge and discharge, as shown in **Fig. S22(b)**. During the charging process, the R_{ct} values decrease initially and then increase. The discharge process is more complicated, with an initial increase, followed by a decrease, and then another increase. Furthermore, the change of R_{ct} is accompanied by a shift in peak positions. To better illustrate the evolving trends, the corresponding contour plot is presented in **Fig. 6(d)** and **Fig. S24(a)**.

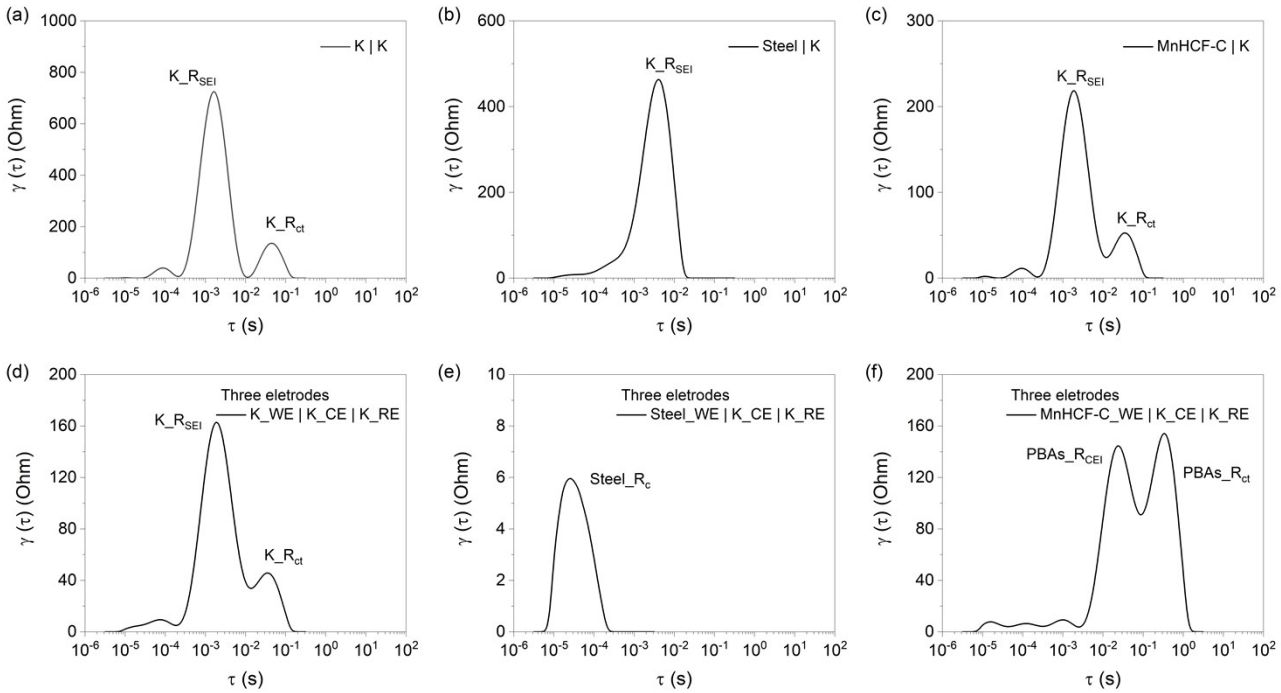

Fig. S23 Identification of related time constant in DRT plots. (a-c) DRT plots obtained using coin cells of K | K, Steel | K, and MnHCF-C | K, respectively. (d-f) DRT plots obtained using three-electrode cells of K_WE | K_CE | K_Re, Steel_WE | K_CE | K_Re, and MnHCF_WE | K_CE | K_Re, respectively.

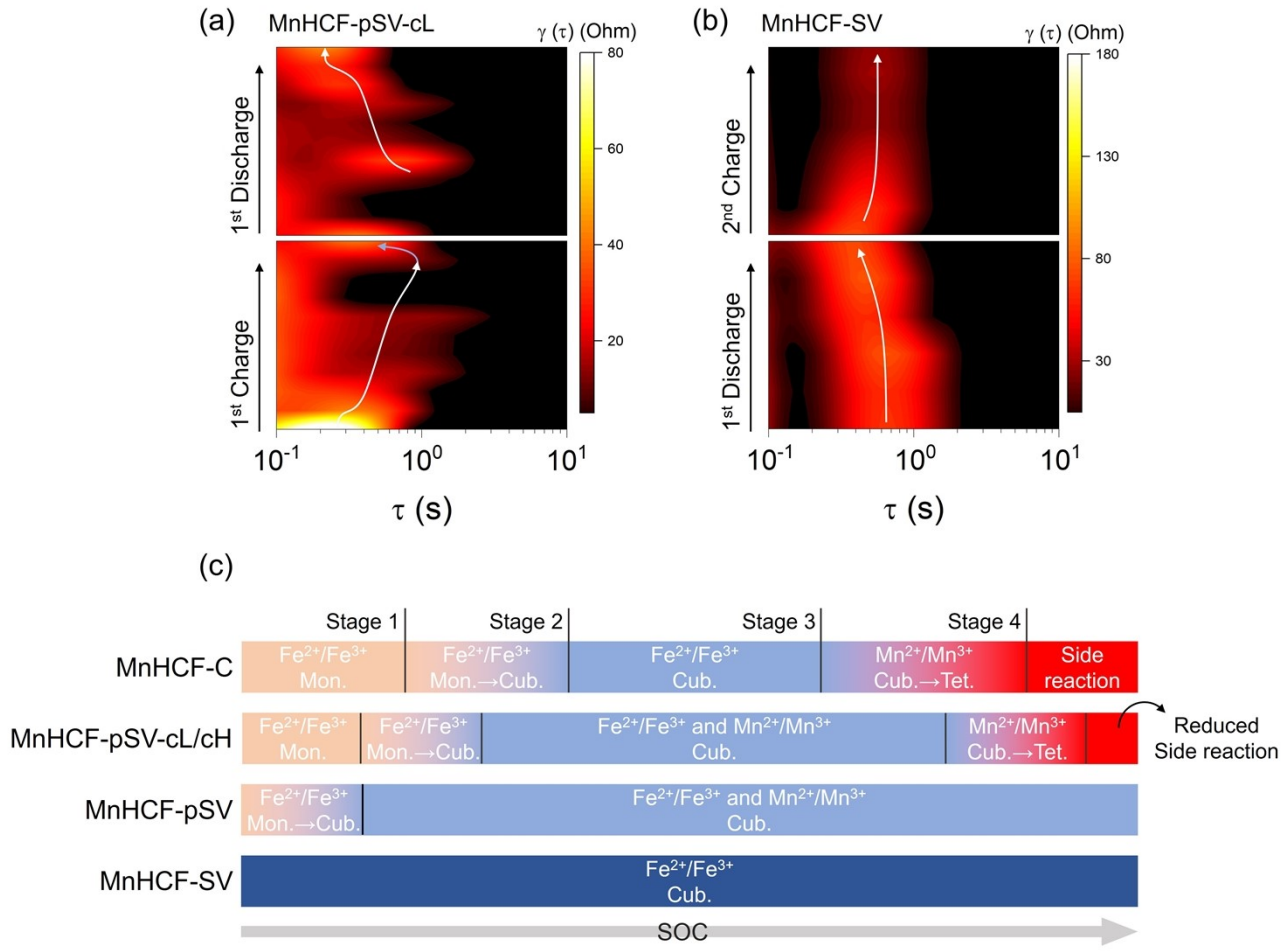

Fig. S24 Contour plots of DRTs for (a) MnHCF-pSV-cL and (b) MnHCF-SV. (c) Summary of the change of DRT peaks.

Table S1. ICP results of the samples.

Sample		K: Mn: Fe	Molecular formula
MnHCF-SV	1st	0.053: 1: 0.676	$K_{0.05}Mn[Fe(CN)_6]_{0.68}\square_{0.32}$
	2nd	0.057: 1: 0.674	$K_{0.06}Mn[Fe(CN)_6]_{0.67}\square_{0.33}$
	3rd	0.055: 1: 0.683	$K_{0.06}Mn[Fe(CN)_6]_{0.68}\square_{0.32}$
MnHCF-IV	1st	1.610: 1: 0.869	$K_{1.61}Mn[Fe(CN)_6]_{0.87}\square_{0.13}$
	2nd	1.660: 1: 0.902	$K_{1.66}Mn[Fe(CN)_6]_{0.90}\square_{0.10}$
	3rd	1.581: 1: 0.845	$K_{1.58}Mn[Fe(CN)_6]_{0.85}\square_{0.15}$
H-MnHCF		1.968: 1: 0.976	$K_{1.97}Mn[Fe(CN)_6]_{0.98}\square_{0.02}$
MnHCF-C		1.855: 1: 0.951	$K_{1.86}Mn[Fe(CN)_6]_{0.95}\square_{0.05}$
MnHCF-pSV-cL		1.643: 1: 0.890	$K_{1.64}Mn[Fe(CN)_6]_{0.89}\square_{0.11}$
MnHCF-pSV-cH		1.636: 1: 0.863	$K_{1.64}Mn[Fe(CN)_6]_{0.86}\square_{0.14}$
MnHCF-pSV		1.641: 1: 0.868	$K_{1.64}Mn[Fe(CN)_6]_{0.87}\square_{0.13}$

Table S2. Refined parameters for H-MnHCF

S.G. P21/n
a=10.10005(21) Å
b=7.32456(9) Å
c=6.96240(10) Å
β=90.0903(16)°
Rw=2.95 %

Atoms	x	y	z	U	Occ.[a]
Fe	0.00000	0.00000	0.00000	0.005	0.9760
Mn	0.00000	0.50000	0.50000	0.005	1.0000
C1	0.56144	0.65787	0.25623	0.010(6)	0.9760
C2	0.95123	0.72545	0.09333	0.010(6)	0.9760
C3	0.69558	0.54344	0.61297	0.010(6)	0.9760
N1	0.49260	0.25389	0.81977	0.038(4)	0.9760
N2	0.02999	0.32968	0.77122	0.038(4)	0.9760
N3	0.20953	0.49731	0.39373	0.038(4)	0.9760
K	0.75624	0.93573	0.47464	0.0201(11)	0.9840

[a] Occupancies are fixed based on the ICP results

Table S3. Refined parameters for MnHCF-IV

S.G. P21/n
a=10.1096(5) Å
b=7.3213(4) Å
c=6.9699(4) Å
β=90.1010(16)°
Rw=2.310 %

Atoms	x	y	z	U	Occ.[a]
Fe	0.00000	0.00000	0.00000	0.0114	0.8690
Mn	0.00000	0.50000	0.50000	0.0370	1.0000
C1	0.53897	0.65317	0.26061	0.0431	0.8690
C2	0.94196	0.75892	0.14396	0.0431	0.8690
C3	0.69712	0.55882	0.56734	0.0431	0.8690
N1	0.45142	0.24641	0.83620	0.0549	0.8690
N2	0.02382	0.35201	0.77982	0.0549	0.8690
N3	0.20143	0.42331	0.38145	0.0549	0.8690
K	0.75096	0.94288	0.47968	0.0318(9)	0.8050

[a] Occupancies are fixed based on the ICP results

Table S4. Refined parameters for MnHCF-SV

S.G. Fm-3m a=10.49870(5) Å Rw=2.694 %					
Atoms	x	y	z	U	Occ.[a]
Fe	0.50000	0.50000	0.00000	0.005	0.6760
Mn	0.50000	0.50000	0.50000	0.005	1.0000
O1	0.50000	0.50000	0.2871(6)	0.0360	0.3240
O2	0.75000	0.25000	0.25000	0.131(3)	0.7921
O3	0.6826(5)	0.3174(5)	0.1826(5)	0.131(3)	0.2079
C	0.50000	0.50000	0.17999	0.0643	0.6760
N	0.50000	0.50000	0.28091	0.0860	0.6760

[a] Occupancies are fixed based on the ICP results of C/N/Fe/Mn atoms. The occupancy of O1 atom, belonging to the coordinated water, was fixed as 1-Occ.(N).

References

1. B. H. Toby and R. B. Von Dreele, *J. Appl. Cryst.*, 2013, **46**, 544-549.
2. B. Ravel and M. Newville, *Phys. Scr.*, 2005, **115**, 1007-1010.
3. H. Funke, M. Chukalina and A. Rossberg, *Phys. Scr.*, 2005, **T115**, 232-234.
4. Z. Shen, L. Cao, C. D. Rahn and C.-Y. Wang, *J. Electrochem. Soc.*, 2013, **160**, A1842-A1846.
5. T. H. Wan, M. Saccoccio, C. Chen and F. Ciucci, *Electrochim. Acta*, 2015, **184**, 483-499.
6. G. Kresse and J. Furthmüller, *Comput. Mater. Sci.*, 1996, **6**, 15-50.
7. B. Hammer, L. B. Hansen and J. K. Nørskov, *Phys. Rev. B*, 1999, **59**, 7413-7421.
8. P. E. Blöchl, *Phys. Rev. B*, 1994, **50**, 17953-17979.
9. L. W. Jiang, Y. X. Lu, C. L. Zhao, L. L. Liu, J. N. Zhang, Q. Q. Zhang, X. Shen, J. M. Zhao, X. Q. Yu, H. Li, X. J. Huang, L. Q. Chen and Y. S. Hu, *Nat. Energy*, 2019, **4**, 495-503.
10. *M. J. e. a. Frisch*, 2009.
11. T. E. Westre, P. Kennepohl, J. G. DeWitt, B. Hedman, K. O. Hodgson and E. I. Solomon, *J. Am. Chem. Soc.*, 1997, **119**, 6297-6314.
12. H. Niwa, T. Moriya, T. Shibata, Y. Fukuzumi and Y. Moritomo, *Scientific Reports*, 2021, **11**.
13. A. Gómez, V. H. Lara, P. Bosch and E. Reguera, *Powder Diffraction*, 2002, **17**, 144-148.
14. W. Zhang, H. Xia, Z. Zhu, Z. Lv, S. Cao, J. Wei, Y. Luo, Y. Xiao, L. Liu and X. Chen, *CCS Chem.*, 2021, **3**, 1245-1255.
15. L. Fan, H. Xie, Y. Hu, Z. Caixiang, A. M. Rao, J. Zhou and B. Lu, *Energy Environ. Sci.*, 2023, **16**, 305-315.
16. Y. Lu, C.-Z. Zhao, J.-Q. Huang and Q. Zhang, *Joule*, 2022, **6**, 1172-1198.
17. V. Vivier and M. E. Orazem, *Chem. Rev.*, 2022, **122**, 11131-11168.